

## Durham Research Online

---

### Deposited in DRO:

12 December 2016

### Version of attached file:

Accepted Version

### Peer-review status of attached file:

Peer-reviewed

### Citation for published item:

Underwood, T. and Erastova, V. and Greenwell, H.C. (2016) 'Ion adsorption at clay mineral surfaces : the Hofmeister series for hydrated smectite minerals.', *Clays and clay minerals.*, 64 (4). pp. 472-487.

### Further information on publisher's website:

<https://doi.org/10.1346/CCMN.2016.0640310>

### Publisher's copyright statement:

### Additional information:

## Use policy

---

The full-text may be used and/or reproduced, and given to third parties in any format or medium, without prior permission or charge, for personal research or study, educational, or not-for-profit purposes provided that:

- a full bibliographic reference is made to the original source
- a [link](#) is made to the metadata record in DRO
- the full-text is not changed in any way

The full-text must not be sold in any format or medium without the formal permission of the copyright holders.

Please consult the [full DRO policy](#) for further details.

1 **Ion Adsorption at Clay Mineral Surfaces: The Hofmeister Series for Hydrated Smectite**

2 **Minerals**

3 Thomas Underwood, Valentina Erastova, H. Chris Greenwell

4 Durham University

5

6 Department of Earth Sciences,

7 Durham University,

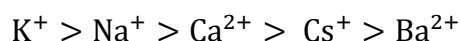
8 Science Labs,

9 Durham DH1 3LE

10  
11  
12  
13  
14  
15  
16  
17  
18  
19  
20  
21  
22  
23  
24  
25  
26  
27  
28  
29  
30

## ABSTRACT

Many important properties of clay minerals are defined by the species of charge-balancing cation. Phenomena such as clay swelling and cation exchange depend upon the cation species present and it is therefore important to understand how the cations bind with the mineral surface at a fundamental level. In the present study, the binding affinities of several different charge-balancing cations with the basal surface of the smectite clay montmorillonite have been calculated using molecular dynamics in conjunction with the well-tempered metadynamics algorithm. The results follow a Hofmeister series of preferred ion adsorption to the smectite basal surfaces of the form:



The results also reveal the energetically favorable position of the ions above the clay basal surfaces. Key features of the free energy profiles are illustrated by Boltzmann population inversions and analyses of the water structures surrounding the ion and clay surface. The results show that weakly hydrated cations ( $K^+$  and  $Cs^+$ ) preferentially form inner-sphere surface complexes (ISSC) above the ditrigonal siloxane cavities of the clay, whilst the more strongly hydrated cations ( $Na^+$ ) are able to form ISSCs above the basal oxygen atoms of the clay surface. The strongly hydrated cations ( $Na^+$ ,  $Ca^{2+}$  and  $Ba^{2+}$ ) preferentially form outer-sphere surface complexes. The results provide insight into the adsorption mechanisms of several ionic species upon smectite clay minerals, and are relevant to many phenomena thought to be affected by cation-exchange, such as nuclear waste disposal, herbicide/pesticide-soil interactions and enhanced oil recovery.

31 *Keywords:* Binding affinity; cation exchange; molecular dynamics; montmorillonite; well-  
32 tempered metadynamics.

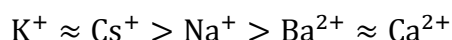
33 **INTRODUCTION**

34 Clays are naturally occurring layered phyllosilicate minerals which are known to play an  
35 important role in many geochemical processes, whether within marine systems, terrestrial soils  
36 or within the subsurface in aquifers and oil reservoirs (Bergaya *et al.*, 2006). Owing to their high  
37 surface area, permanent negative charge and cation exchange properties, smectite clay minerals  
38 have found an increasing multitude of practical applications and have been extensively studied  
39 using analytical laboratory based techniques. In recent years, computational techniques, such as  
40 molecular dynamics (MD) and *ab-initio* calculations (including density functional theory –  
41 DFT), have become increasingly beneficial in helping improve our understanding of clay mineral  
42 properties at the atomistic level ((Greenwell, 2006), (Suter J. L., 2009)).

43 Three types of clay mineral surfaces are apparent: (i) the external basal surfaces, (ii) the  
44 external clay edges; (iii) the interlayer basal surfaces. The adsorption and exchange of cations at  
45 the different clay minerals surfaces can comprehensively alter the physical and chemical  
46 properties of the clay mineral. Interlayer bound potassium, for example, acts as a swelling  
47 inhibitor, preventing hydration and expansion of the interlayer region, whilst sodium promotes  
48 swelling when present in smectite-like clay minerals (Boek *et al.*, 1995). Furthermore, owing to  
49 their use as a barrier material in underground nuclear waste repositories it is becoming  
50 increasingly important to understand how radioactive cations, such as barium and cesium, adsorb  
51 to clay mineral surfaces, with potentially significant ramifications for nuclear waste repository  
52 design and operation (Ngouana *et al.*, 2014). Since the behavior of clay minerals depend upon  
53 the species of charge-balancing cation, it is important to understand how the cation binds with  
54 the mineral surface, and how the cation's affinity to the surface differs from ion to ion; however,  
55 studying the behaviour of cations at clay mineral surfaces and within interlayers is particularly

56 challenging. Nuclear magnetic resonance (NMR) studies have been undertaken on non-  
57 paramagnetic synthetic clays offering insight on ion dynamics and distribution (Bowers *et al.*,  
58 2008), while the use of quasi-elastic neutron scattering (QENS) on well-ordered vermiculite clay  
59 gels, as well as smectites, has allowed the study of cation/water structure in interlayers  
60 ((Swenson *et al.*, 2000 ), (Marry *et al.*, 2013)). Additional insight into swelling energetics and  
61 structure has been obtained from computer simulation of hydrated clay minerals ((Boek *et al.*,  
62 1995), (Shroll and Smith, 1999), (Boek and Sprik., 2003)).

63 A key property of many clay minerals is cation-exchange, where a more labile cation is  
64 substituted by a less labile one to modify the clay mineral activity. The traditional view of  
65 alkaline metal ion selectivity for cation-exchange follows a Hofmeister-like series (Hanshaw,  
66 1964):



67 The reasoning for this sequence have been postulated through (at least) two arguments:

- 68 1) The ratio of hydrated cation size to interlayer spacing ((Gast, 1969), (Gast, 1972)),  
69 whether the hydrated ion can fit within the steric cavities of the interlayer spacing;
- 70 2) The cations' ability to partially dehydrate at the mineral surface and thus form strong  
71 inner-sphere surface complexes (Eisenman, 1962).

72

73 Whilst many historical studies of the Hofmeister series have examined the hydration  
74 properties of the ions, in recent years it has become increasingly apparent that ion-  
75 macromolecule interactions also play a dominant role (Zhang and Cremer, 2006).

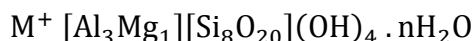
76 Previous computational work has been able to elucidate some of the properties of cation-  
77 exchange clay systems. It has previously been shown that whilst the binding energy between

78 potassium and montmorillonite is greater than that between cesium and montmorillonite, the  
79 cesium-montmorillonite system is overall more stable due to the decreased enthalpy of hydration  
80 of the potassium over the cesium in the solvent phase (Teppen and Miller, 2006). The result  
81 shows it is important to consider not only the effect of the ion interacting with the mineral  
82 surface, but also with the bulk solvent phase. Previously, this has been achieved using an explicit  
83 solvent bath (Rotenberg *et al.*, 2007) or through the use of thermodynamic cycles (Rotenberg *et*  
84 *al.*, 2009).

85         In this present study, classical molecular dynamic simulations have been used in  
86 conjunction with well-tempered metadynamics to determine the free energy of adsorption of, as  
87 well as the competition between, cations at the hydrated basal surfaces of the smectite clay  
88 mineral montmorillonite. The following simulations are particularly pertinent for understanding  
89 of the phenomenon of multicomponent cation-exchange during low salinity enhanced oil  
90 recover, whereby organic matter, bridged to the surface through divalent cations, becomes  
91 desorbed from the basal surface of a clay mineral (Underwood *et al.*, 2015).

92 **METHODS**93 ***Model Setup***

94 The clay unit cell used in this study was a Wyoming-like montmorillonite with atomic  
95 coordinates taken from the *American Mineralogist Crystal Structure Database* ((Downs and  
96 Hall-Wallace, 2003), (Viani *et al.*, 2002)) and with stoichiometry:



97 In this model the octahedral sheets of the clay contained one Mg atom for every three Al atoms,  
98 whilst both tetrahedral sheets contained no isomorphous substitutions. The resulting unit cell  
99 possessed a single net negative charge, corresponding to a surface charge density of  
100 approximately  $0.35 \text{ C m}^{-2}$ . Periodically replicated super-cells were generated containing one  
101 layer of montmorillonite, composed of 18 unit cells (6 x 3 x 1), with dimensions of  
102 approximately 30 x 30 x 100 Å, and a pore-spacing of approximately 90 Å (Figure 1).  
103 Montmorillonite structures initially occupied the region  $0 < z < 7 \text{ Å}$  in all the following  
104 simulations, and the clay position varied little over all timescales modelled. The simulation  
105 super-cells were subsequently hydrated (with approximately 2500 water molecules) and the  
106 requisite number of cations added to the system to charge balance the montmorillonite surface.  
107 In total, five independent systems were set up differing according to the type of charge-balancing  
108 cation. The cations considered in this study were: sodium ( $\text{Na}^+$ ), potassium ( $\text{K}^+$ ), cesium ( $\text{Cs}^+$ ),  
109 calcium ( $\text{Ca}^{2+}$ ) and barium ( $\text{Ba}^{2+}$ ).

110 The clay mineral has been modelled using the ClayFF force field (Cygan *et al.*, 2004),  
111 which is specifically parameterized to model layered minerals. The ClayFF force field is  
112 designed such that the entire interactions within, and structure of, the clay is described wholly by  
113 the non-bonded Lennard-Jones and Coulomb potentials (hydroxyl groups are bonded as an



114 exception). The standard SPC water model (Berendsen *et al.*, 1987) has been used to  
115 parameterize the solvent. Ion parameters are taken from a variety of sources and are consistent  
116 with the ClayFF and SPC force fields ((Smith and Dang (I), 1994), (Smith and Dang (II), 1994)  
117 (Koneshan *et al.*, 1998),(Aqvist, 1990)), (Cygan *et al.*, 2004).

118

### 119 ***Equilibration Details***

120 All simulations have been initialized with an energy minimization run to reduce any  
121 excessive force on any one atom. This was accomplished using a steepest descents algorithm,  
122 with convergence achieved once the maximum force on any one atom was less than  $10 \text{ kJ mol}^{-1}$   
123  $\text{\AA}^{-1}$ . Subsequently, equilibration simulations were run for a 10 ns period in the constant number  
124 of particles, pressure and temperature (NPT) ensemble at 300 K and 1 bar using a velocity-  
125 rescale Berendsen thermostat, temperature coupling constant set to 0.1 ps, and a semi-isotropic  
126 Berendsen barostat, with pressure-coupling constant 1 ps. The Berendsen thermostat and barostat  
127 offered swift equilibration of the system, and convergence was adjudged to have been attained  
128 once both the  $z$ -spacing and potential energy had converged.

129

### 130 ***Metadynamic Details***

131 Subsequent to equilibration, the super-cell was translated along the  $z$ -axis such that the  
132 apical oxygen atoms of the silicate sheet of the lowest clay basal surface lay upon the  $z = 0 \text{ \AA}$   
133 plane. Before any free energy calculations were carried out, the clay model was fixed in place as  
134 a rigid structure. Subsequently, a single cation was chosen at random to be the test ion, upon  
135 which the free energy calculations have been performed. All other ions in the system were free to  
136 move according to the force fields used in the simulations.

137           The well-tempered metadynamics algorithm was used to explore the free energy curve of  
138 the clay-ion-water system as a function of the clay-ion separation (i.e. the reaction coordinate).  
139 During the metadynamics simulation the forces calculated with conventional molecular  
140 dynamics are modulated by adding Gaussian functions to the Hamiltonian at points along the  
141 reaction coordinate (Barducci *et al.*, 2008). Here, twenty-five separate well-tempered  
142 metadynamic simulations were run, five for each cation type. It is important to run multiple  
143 ensemble simulations when calculating equilibrium thermodynamic properties, such as binding  
144 energies, since any one simulation is unlikely to sufficiently sample all of the phase-space  
145 required to satisfy the ergodic hypothesis (Coveney and Wan, 2016). Five separate ensemble  
146 simulations were deemed sufficient to reduce the total uncertainty in the free energy profiles  
147 generated using the metadynamic algorithm in this work. Each metadynamic simulation was run  
148 for a duration of 200 *ns* at 300 *K* in the constant number of particles, volume and temperature  
149 (NVT) ensemble. Gaussian functions with an initial height of 1.20 *kJ/mol*, a width of 0.10 Å, and  
150 a bias factor of 10 were applied to the Hamiltonian every 0.5 *ps*. Convergence of the well-  
151 tempered metadynamics algorithm was ensured by observing that the Gaussian height tended to  
152 zero throughout all well-tempered metadynamic simulations. Checks were also made to ensure  
153 that the test ion sampled all of the available planar *xy*-space, in conjunction with clay-ion  
154 separation space.

155           Due to the translational symmetry of the clay mineral, additional bias potentials were  
156 added to the test ion. This constrained the ion within a single unit cell of the montmorillonite  
157 surface. Any additional sampling would simply increase computational time, yet yield no  
158 additional information. This constraint was achieved using a spring-like bias of the form:

159                           
$$V_{\text{wall}}(x) = k(x - x_{\text{max}})^4 \quad \text{for } x > x_{\text{max}} \quad (1)$$

160 where  $k$  is the elastic spring constant of the wall, set to  $500 \text{ kJ/mol}$ , and  $x_{max}$  is the lower limit of  
161 the wall. Similar boundaries were setup to constrain the lower bounds of the test ion in the  $x$ -  
162 direction, to constrain the ion in the  $y$ -direction, as well as to keep the test ion within  $10 \text{ \AA}$  of the  
163 mineral surface.

164

### 165 ***Simulation Details***

166 All MD simulations were performed using GROMACS version 4.6.7 (Pronk, et al., 2013)  
167 with the Particle-Mesh-Ewald summation method for determining the electrostatic contribution,  
168 with a real-space electrostatic cut-off of  $12 \text{ \AA}$ , a reciprocal space precision of  $10^{-5}$ , in addition to  
169 a van der Waals cut-off distance of  $1.2 \text{ \AA}$ . The well-tempered metadynamic algorithm has been  
170 implemented using PLUMED 2.1.2 (Bonomi *et al.*, 2009) (Tribello *et al.*, 2014), which works in  
171 conjunction with GROMACS, whilst all images of the simulated structures have been produced  
172 using VMD 1.9.2 (Humphrey, 1996).

173

### 174 ***Analysis Details***

175 All free energy analyses have been carried out using the internal tools for GROMACS  
176 4.6.7 and PLUMED 2.1.2 (Bonomi *et al.*, 2009) (Tribello *et al.*, 2014). The Python module  
177 MDAnalysis 0.13 (Michaud-Agrawal *et al.*, 2011) and Matplotlib 1.5.1 (Hunter, 2007) were used  
178 to further analyze simulation trajectories and generate figures of water densities and radial  
179 distribution functions (RDFs). The plotted free energy profiles present the average free energy at  
180 each point along the reaction coordinate as a bold line and the relative error (plus-minus) is  
181 presented in the shaded area. The values of individual binding energies are given with the  
182 corresponding standard error as plus-minus. All ion density profiles (dotted lines in the free

183 energy profiles) have been calculated using the last 5 *ns* of the 10 *ns* equilibration period, i.e.  
184 from an unbiased simulation.

185

**RESULTS**

186

It is initially worth highlighting the general shape of the free energy curves (Figure 2).

187

After a short range repulsion between ion and mineral surface, and beyond (often several)

188

minima, the free energy profiles plateau. In the long clay-ion separation limit, this plateau can be

189

decomposed as a combination of clay ( $F_{\text{self}}^{\text{clay}}$ ), ion ( $F_{\text{self}}^{\text{ion}}$ ) and solvent ( $F_{\text{self}}^{\text{water}}$ ) self-energies; clay-

190

water ( $F_{\text{hydration}}^{\text{clay}}$ ) and ion-water ( $F_{\text{hydration}}^{\text{ion}}$ ) hydration energies; as well as long-range

191

interaction terms ( $F_{\text{electrostatic}}^{\text{clay-ion}}$ ). Namely the binding free energy ( $F$ ), can be expressed as:

192

$$\lim_{z \rightarrow \infty} F(z) = F_{\text{self}}^{\text{clay}} + F_{\text{self}}^{\text{ion}} + F_{\text{self}}^{\text{water}} + F_{\text{hydration}}^{\text{clay}} + F_{\text{hydration}}^{\text{ion}} + F_{\text{electrostatic}}^{\text{clay-ion}}(z) \quad (2)$$

193

This means that the overall binding energy ( $\Delta F_{\text{Binding}}$ ) of the ion to the surface can be calculated

194

as:

195

$$\Delta F_{\text{Binding}} = F(z_{\text{min}}) - \lim_{z \rightarrow \infty} F(z) \quad (3) \text{ where } z_{\text{min}} \text{ is the location of the global energy}$$

196

minimum with respect to clay-ion separation.

197

Note that at sufficiently large  $z$ , the individual self-energies of the unbound system and hydration

198

terms in equation 2 are independent of  $z$ , since the hydration shells of the ion and clay no longer

199

overlap. Thus, at large  $z$ , when comparing binding energies between different ion species, one

200

needs only to consider the difference between the long-range clay-ion electrostatic term. Since

201

all simulations have been run at the same temperature (300 K) and ionic strengths the long-range

202

electrostatic term, which can be described through Poisson-Boltzmann theory, is postulated to be

203

equal for all different ions at any arbitrary  $z$ . It is therefore justified to normalize the free energy

204

profiles subject to the boundary condition that for large clay-ion separation:

205  $\lim_{z \rightarrow \infty} F(z) = 0$  (4) Following this argument, a direct comparison of  
206 the binding free energies differences between dissimilar species of monovalent and divalent  
207 cations have been calculated (Table 1).

208

### 209 ***Free Energy Profiles:***

210 The free energy profile for all the systems considered (Figure 2), highlight several points  
211 of interest along the reaction-coordinate. These are highlighted by the points (A), (B), (C), (D)  
212 and (E) across the top of the figure. To be consistent, the points correspond to the coordination  
213 states of the ion. In brief, (A) corresponds to a primary inner-sphere surface complex (ISSC); (B)  
214 corresponds to a secondary ISSC; (C) corresponds to outer-sphere surface complex (OSSC) and  
215 (D) corresponds to a secondary hydration shell surface complex (SHSSC). These terms shall be  
216 explained in the following sections. The point (E) corresponds to a clay-ion separation of 10 Å,  
217 the maximal distance of the reaction-coordinate in the metadynamic simulations.

218

### 219 ***Na-Montmorillonite:***

220 The free energy profile for the sodium-montmorillonite system (Figure 2 - Na) shows that  
221 at close separation distances (less than 2 Å) the montmorillonite-ion interaction is entirely  
222 repulsive. This represents the close-range repulsion between clay and ion due to electron wave-  
223 function overlap. Beyond this, the ion experiences three individual clay-ion separations of  
224 (meta)stable equilibria. The global minimum, and thus the most energetically favorable  
225 montmorillonite-sodium separation is at 3.8 Å, with a binding energy of  $-9.00 \pm 0.35$  kJ/mol  
226 (Figure 2 – Na(C)). A secondary, metastable minimum, is located nearer to the clay surface, at a  
227 clay-sodium distance of 2.3 Å, with a binding energy of  $-2.76 \pm 0.43$  kJ/mol (Figure 2 - Na(B)). A

228 third, metastable minimum, is located further from the clay surface, at a separation value of 6 Å  
229 and with a binding energy of  $-3.68 \pm 0.37$  kJ/mol (Figure 2 - Na(D)).

230 The global minimum corresponds to a system where the sodium cation is fully hydrated,  
231 and the ion's solvation shell is associated to the mineral surface *via* hydrogen bonding. This can  
232 be observed in the overlapping water structures of the first hydration shell of the ion with the  
233 first hydration layer of the clay (Figure 3 - Na(C)). This phenomenon is well known, and referred  
234 to as an outer-sphere solvation complex (OSSC). In contrast, the metastable minimum nearer the  
235 clay surface corresponds to an inner-sphere solvation complex (ISSC), whereby the cation is  
236 only partially hydrated, and is directly adsorbed to the mineral surface *via* electrostatic  
237 interactions (Figure 3 - Na(B)). The metastable minimum farthest away from the clay surface  
238 corresponds to where the second hydration shell of the sodium ion overlaps with the first  
239 hydration layer of the clay (Figure 3 - Na(D)). This situation is observed for several cations and  
240 shall be hereafter denoted as a secondary hydration shell surface complex (SHSSC). Also  
241 presented is the water structure surrounding the ion and clay at a clay-ion separation of 10 Å  
242 (Figure 3 - Na(E)). It can be noted that at such distance, the hydration layers of the clay and ion  
243 no longer overlap.

244 The radial distribution functions (RDFs) between sodium ion and water/basal clay  
245 oxygen further reiterate that the minima correspond to ISSC and OSSC. It can be seen that for  
246 the ISSC (Figure 4 - Na(B)), the basal clay oxygen atoms are shared with water oxygen atoms in  
247 the first coordination shell of the ion. In contrast, for the OSSC (Figure 4 - Na(C)), the basal clay  
248 oxygen atoms are contained within the second coordination shell of the ion. For the SHSSC  
249 (Figure 4 - Na(D)), the clay basal oxygen atoms contribute to the third coordination shell of the  
250 sodium ion. Also presented is the RDF for the system at a clay-ion separation of 10 Å (Figure 4 -

251 Na(E)). In this case the hydration layers of the ion and clay no longer interact and the resulting  
252 RDF is that of the sodium ion with bulk water.

253         The planar density of the ion above the mineral surface shows that, for the ISSC, the  
254 sodium ion is extremely localized above a single basal clay oxygen (Figure 5 - Na(B)). In  
255 contrast, the OSSC is less localized above the clay basal surface (Figure 5 - Na(C)), with a  
256 preference to be located above one of the hexagonal siloxane cavities of the mineral surface. For  
257 the SHSSC and beyond, the ion's position above the basal clay surface is no longer localized,  
258 and is homogeneously dispersed across the unit cell (Figure 5 - Na(C) and Na(D)).

259

260 ***K-Montmorillonite:***

261         The free energy profile for potassium (Figure 2 - K) presents several features similar to  
262 that of sodium. Again, it can be seen that beyond the typical close distance repulsion, three  
263 separate (meta)stable minima are observed. The global minimum, in this instance, is located near  
264 the surface of the mineral, at a montmorillonite-potassium separation of 1.3 Å, with a binding  
265 energy of  $-10.56 \pm 1.29$  kJ/mol (Figure 2 - K(A)). The next most stable minimum is located at 4.7  
266 Å, with a binding energy of  $-3.83 \pm 0.37$  kJ/mol (Figure 2 - K(C)). There is also a metastable  
267 minimum between these two points at a clay-potassium separation of 2.6 Å with a binding  
268 energy of  $-2.46 \pm 0.70$  kJ/mol (Figure 2 - Na(B)).

269         Focusing on the global energy minimum (point A), both the water structure (Figure 3 -  
270 K(A)) and the RDF (Figure 4 - K(A)) reveal that the ion forms an ISSC in its most energetically  
271 favorable state. In particular, the RDF shows that the first coordination shell of the potassium ion  
272 is largely composed of clay oxygen atoms. The *xy*-planar density of the potassium ion in its ISSC  
273 state (Figure 5 - K(A)) shows that the ion is extremely localized above the hexagonal cavities of



274 the clay surface. This behavior is in contrast to the ISSC observed for sodium. The terms primary  
275 ISSC and secondary ISSC are here introduced to denote the difference between these two  
276 different forms of ISSC. A primary ISSC denotes an ion that sits above one of the hexagonal  
277 cavities of the clay surface, whilst the term secondary ISSC denotes that the ion sits above one of  
278 the basal oxygen atoms of the clay.

279 The least energetically favorable metastable minimum is located at point (B) in the free  
280 energy profile (Figure 2 – K(B)). The water structure (Figure 3 - K(B)) and RDF (Figure 4 –  
281 K(B)) indicate that this minimum is also an ISSC. The  $xy$ -planar density of the ion above the  
282 surface (Figure 4 - K(B)) indicates that this is a secondary ISSC. The results show that potassium  
283 can stably form both primary, and secondary, inner-sphere surface complexes.

284 The most energetically favorable metastable minimum is located at point (C) in the free  
285 energy profile (Figure 2 – K(C)). Here the potassium ion forms an OSSC, as the first hydration  
286 shell of the ion overlaps with the first hydration layer of the clay (Figure 3 - K(C)). The RDF  
287 (Figure 4 - K(C)) also highlights that the basal clay oxygen atoms coordinate within the second  
288 hydration shell of the potassium cation. Like the sodium ion, the OSSC of potassium is loosely  
289 localized above the hexagonal siloxane cavities of the basal surface, as evidenced by the  $xy$ -  
290 planar density distribution (Figure 5 - K(C)). Beyond this point, the potassium ion is not  
291 observed to form a SHSSC and moves freely across the  $xy$ -plane (Figure 5 - K(E)).

292

### 293 ***Cs-Montmorillonite:***

294 The free energy diagram for the cesium-montmorillonite system (Figure 2 - Cs) is very  
295 similar to that of potassium. Again, three separate minima are observed. The global energy  
296 minimum is at a montmorillonite-cesium separation of 2.0 Å with a binding energy of -

297  $8.34 \pm 0.40 \text{ kJ/mol}$  (Figure 2 - Cs(A)). The secondary minimum is at a clay-ion distance of  $2.7 \text{ \AA}$   
298 with a binding energy of  $-7.51 \pm 0.38 \text{ kJ/mol}$  (Figure 2 - Cs(B)) and the tertiary minimum is  
299 located at a clay-ion distance of  $4.6 \text{ \AA}$  with a binding energy of  $-4.64 \pm 0.26 \text{ kJ/mol}$  (Figure 2 -  
300 Cs(C)).

301 The global minimum of cesium forms an ISSC as can be observed through the water  
302 structure (Figure 3 - Cs(A)) and cesium-oxygen RDF results (Figure 4 - Cs(A)). Like potassium,  
303 the global energy minimum of cesium is localized above the hexagonal siloxane cavities of the  
304 clay surface (Figure 5 - Cs(A)) and is therefore observed to form primary ISSCs.

305 The second and third minima of cesium correspond to a secondary ISSC and OSSC  
306 respectively. This is evidenced by the overlapping of the water structures surrounding the ion  
307 and clay (Figure 3 - Cs (B) and Cs(C)), the overlapping oxygen atoms in the RDFs (Figure 4 -  
308 Cs(B) and Cs(C)), as well as the ion localizations above the  $xy$ -plane (Figure 5 - Cs(B) and  
309 Cs(C)). Much like potassium therefore, cesium readily forms both secondary ISSCs and OSSCs.  
310 Unlike potassium however, the secondary ISSC is more energetically stable than the OSSC.

311

### 312 ***Ca-Montmorillonite:***

313 In contrast with the results for other ions presented so far, the free energy profile for  
314 calcium shows only one stable minimum (Figure 2 – Ca). This minimum is at a clay-ion distance  
315 of  $3.8 \text{ \AA}$  and has a binding energy of  $-16.76 \pm 0.41 \text{ kJ/mol}$  (Figure 2 - Ca(C)). The water structures  
316 surrounding the calcium and clay in conjunction with the RDFs between ion and oxygen atoms  
317 show that this global energy minimum is an OSSC. The water structure (Figure 3 – Ca(C))  
318 shows that the first hydration shell of the calcium overlaps with the first hydration layer of the  
319 clay basal surface. Furthermore, the RDF (Figure 4 - Ca(C)) indicates that the basal oxygen

320 atoms of the clay contribute to the second hydration shell of the calcium. The planar density of  
321 the calcium ion in its global OSSC state (Figure 5 - Ca(C)) presents that the calcium ion sits  
322 above the hexagonal siloxane cavities of the basal surface of the clay, in agreement with the  
323 trends observed for the monovalent ions. Nonetheless, the OSSC for the calcium ion is more  
324 localized compared to the OSSCs for monovalent ions.

325 Point (D) in the calcium system refers to the sudden change in gradient of the free energy  
326 curve. This change in gradient is due to the completion of the second hydration shell of the  
327 calcium ion as is shown in the water density profile (Figure 3 - Ca(D)). At this point the clay no  
328 longer contributes to the hydration shells of the calcium ion, as is confirmed by comparing the  
329 RDF between calcium and basal clay oxygen atoms with the RDF between calcium and all  
330 oxygen atoms (Figure 4 - Ca(D)). The planar density profile for point (D) (Figure 4 - Ca(D))  
331 shows that calcium ion sits above the either the basal oxygen of silicon atoms of the clay.  
332 Therefore, the aforementioned completion of the second coordination shell of the calcium ion is  
333 achieved with water oxygen atoms.

334

### 335 ***Ba-Montmorillonite:***

336 The free energy profile of the montmorillonite-barium system (Figure 2 - Ba) presents  
337 several interesting features not observed in the free energy profile for calcium. The global energy  
338 minimum (point C) corresponds to a clay-ion separation of 4.2 Å with a binding energy of -  
339  $16.66 \pm 1.46 \text{ kJ/mol}$  (Figure 2 - Ba(C)). There is also a second, energetically expensive,  
340 metastable minima in the free energy curve (point A). This metastable minimum is located at a  
341 clay-ion separation value of 1.9 Å and has a binding energy of  $+18.26 \pm 3.55 \text{ kJ/mol}$  (Figure 12 -  
342 Ba(A)), i.e. energy is required to place the ion into this metastable minimum. Two plateaus can

343 also be seen in the free energy profile of barium. Point (B) is at a clay-ion separation of 2.6 Å  
344 and has a binding energy of  $-0.54 \pm 1.82$  kJ/mol (Figure 2 - Ba(B)), whilst point (D) is at a clay-  
345 ion separation of 5.8 Å and has a binding energy of  $-8.38 \pm 1.25$  kJ/mol (Figure 2 - Ba(D)).

346 The water density profiles and RDFs of the barium-montmorillonite system explain how  
347 the ion binds with the mineral surface. At points (A) and (B), the ion is directly coordinated by  
348 basal oxygen atoms, forming primary and secondary ISSCs respectively (Figures 3 and 4 –  
349 Ba(A) and Ba(B)). The water structure shows that the global energy minimum occurs when the  
350 barium ion is an OSSC (Figure 3 - Ba (C)). In such an occurrence, the basal oxygen atoms of the  
351 clay contribute to the second hydration shell of the cation, as can be seen in the corresponding  
352 RDF (Figure 4 - Ba(C)). The plateau at point (D) of the free energy curve occurs when the  
353 second hydration layer of the barium ion begins to completely coordinate with water oxygen  
354 atoms (Figure 3 - Ba(D)).

355 Analysis of the planar density of barium above the  $xy$ -plane of the clay shows that the  
356 two ISSCs are extremely localized above a cavity of the clay siloxane (Figure 5 - Ba (A)) or  
357 directly above basal oxygen atoms (Figure 5 - Ba (B)) for the metastable minimum (point A) and  
358 plateau (point B) respectively. Similar to all other OSSCs, the OSSC of barium is localized  
359 above one of the hexagonal siloxane cavities of the clay (Figure 5 - Ba (C)), whilst at all clay-ion  
360 separations greater than this distance, the cation freely traverses across the  $xy$ -plane of the clay  
361 mineral (Figure 5 - Ba (D)).

362

363

## DISCUSSION

364

365 The results show that the charge-balancing cations of montmorillonite can form four  
different stable surface complexes: a primary ISSC located above the siloxane cavity of the basal

366 clay surface; a secondary ISSC located above a basal oxygen atom; an OSSC loosely located  
367 above siloxane cavity; and a SHSSC, which is due to the overlap of the ion's second hydration  
368 sphere with the clay minerals first hydration layer. No further surface complexes were observed  
369 in the simulations.

370         The formation of two separate ISSCs has been noted in the literature previously. In  
371 particular, it has been shown that weakly hydrated interlayer cations ( $K^+$ ,  $Cs^+$ ) form ISSCs above  
372 the siloxane cavity of the clay interlayer ((Park and Sposito, 2002), (Nakano *et al.*, 2003), (Marry  
373 and Turq, 2003)) whilst strongly hydrated cations ( $Na^+$ ) form ISSCs on tetrahedral charge sites  
374 ((Boek *et al.*, 1995), (Chang *et al.*, 1995), (Marry and Turq, 2003)). The results presented here  
375 supplement this previous work, and further suggest that the formation of ISSCs for strongly  
376 hydrating cation can occur in the absence of tetrahedral charge substitutions. Moreover, they  
377 implicate that the formation of different surface complexes is related to the hydration properties  
378 of the cation. The stable surface complexation of a cation is related to the hydrated radii of the  
379 atom, which is, in turn, inversely proportional to the charge/size ratio of the ion (Table 2).

380         The weakly hydrated cations,  $K^+$  and  $Cs^+$ , have very similar hydration radii (Table 2), and  
381 therefore exhibit similar behavior. In both cases, the primary ISSC is the most energetically  
382 favorable state of the ion, and the secondary ISSC and OSSC are metastable. The strongly  
383 hydrated monovalent cation,  $Na^+$ , forms secondary ISSCs, OSSCs and SHSSCs, and is  
384 energetically most stable in its OSSC. Similarly, divalent cations form globally stable OSSCs, in  
385 concordance with the relevant literature ((Brown and Kevan, 1988), (Papelis and Hayes, 1996),  
386 (Chen and Hayes, 1999), (Strawn and Sparks, 1999), (Greathouse *et al.*, 2000)). Barium exhibits  
387 interesting behaviour; it is an ion that can form stable primary ISSCs and OSSCs, with plateaus  
388 in the free energy profile associated with the formation of a secondary ISSC and a SHSSC

389 (Zhang *et al.*, 2001). This is due to the larger atomic radius of barium compared to calcium,  
390 whereby the charge/size ratio of barium lies somewhere between that of calcium and sodium.

391 Overall, the results are well converged. The largest errors encountered are for the free  
392 energy profiles of potassium and barium. Since the free energy profile for barium contains  
393 several plateaus and minima, the metadynamic algorithm requires more simulation time to  
394 sample all clay-ion separation phase space compared to other ions. The potassium ion contains a  
395 large error due to the lack of convergence in the global energy minimum. This is due to the  
396 complex coordination of oxygen atoms to the potassium ion, and shall be elaborated upon further  
397 in the following sections.

398

#### 399 ***Accuracy of Results:***

400 To further analyze the accuracy of the free energy profiles, a comparison is made  
401 between the equilibrium density profile of the unbiased equilibration simulation with the density  
402 profile derived from the free energy. The cation density surrounding the montmorillonite surface  
403 is derived from the free energy profile as:

$$404 \quad n(d) \propto \exp\left(\frac{-\Delta G(d)}{k_B T}\right) \quad (5) \text{ where } n(d) \text{ is the density profile of the ion}$$

405 surrounding the clay,  $\Delta G(d)$  is the corresponding free energy at the point  $d$  and  $k_B T$  is the  
406 thermal energy at temperature  $T$ . Strictly speaking, since the simulations have been carried out in  
407 the NVT ensemble, the calculated free energy is the Helmholtz free energy. However, because  
408 the simulations had been previously equilibrated in the NPT ensemble, one can assume that the  
409 Helmholtz and Gibbs free energies are equivalent, under the assumption that the metadynamic  
410 bias applied to the ion does not alter the average  $z$ -spacing of the simulation box.

411           The analysis shows that the free energy profiles capture the overall trends observed in the  
412 unbiased density profile (Figure 6). In particular, the strongly hydrating cations ( $\text{Na}^+$ ,  $\text{Ca}^{2+}$  and  
413  $\text{Ba}^{2+}$ ) density profiles match extremely well. The free energy profiles generated for  $\text{Na}^+$ ,  $\text{Ca}^{2+}$   
414 and  $\text{Ba}^{2+}$  capture the essential details of the equilibrium density profile and agrees with previous  
415 results of cationic distribution surrounding montmorillonite basal surfaces (Rotenberg *et al.*,  
416 2010) (Greathouse *et al.*, 2015). The ion densities calculated from the free energy profiles for the  
417 weakly hydrating cations ( $\text{K}^+$  and  $\text{Cs}^+$ ) vary considerably compared to the equilibrium density. In  
418 the case of potassium, the metadynamic density underestimates the the proportion of secondary  
419 ISSCs and OSSCs, suggesting that the free energy calculation overestimates the global binding  
420 energy of potassium to montmorillonite. In contrast, the metadynamic density overestimates the  
421 proportion of secondary ISSCs and OSSCs for cesium. This suggests that the free energy profile  
422 underestimates the global binding energy of cesium. Clearly, there is a phenomenon occurring  
423 for the weakly hydrated cations, causing their binding energies to be less accurate compared to  
424 their more strongly hydrated counterparts.

425

### 426 **Coordination Analysis**

427           The lower accuracy in the binding energies for potassium and cesium can be explained by  
428 examining the coordination number of the ion in its most energetically stable state. This is  
429 calculated by integrating under the first peak of the radial distribution function (RDF) for each  
430 ion (Table 3). Note that in bulk, the coordination of ions ranges between 6 to 8 oxygen atoms,  
431 systematically 1 to 2 counts over the expected literature values (Varma, 2006). In the SHSSC  
432 and OSSC states, the ion remains completely coordinated with water oxygen atoms. In the  
433 secondary ISSC the strongly hydrated sodium ion is coordinated by five water oxygen atoms and

434 one clay oxygen atom. This, along with the  $xy$ -planar density for sodium in its ISSC, proves that  
435 the strongly hydrated monovalent cation coordinates directly above a single basal clay oxygen  
436 atom. The coordination of the secondary ISSCs for the weakly hydrating cations, potassium and  
437 cesium, show that 2 to 3 clay oxygen atoms are contained within the ions first coordination shell.  
438 The secondary ISSCs for potassium and cesium complex with a triad of basal oxygen atoms, in  
439 keeping with previous literature (Park and Sposito, 2002).

440 Profoundly, for the primary ISSC of potassium and cesium, the ion is coordinated with  
441 six oxygen clay atoms, as well as four/six water oxygen atoms. This drastic change in the total  
442 coordination number of potassium and cesium is the reason that the binding energy calculations  
443 are less precise for these ions. It is believed that the structure of the basal siloxane surface is  
444 formed of ditrigonal cavities (Tesson *et al.*, 2016), rather than the hexagonal cavities observed in  
445 these simulations. This suggests a limitation in the force field used within these calculations. The  
446 recently developed polarizable force field (Tesson *et al.*, 2016) is parameterized to accurately  
447 reproduce the ditrigonal structure of a clay mineral surface, and may be a more suitable choice  
448 going onwards with further binding energy calculations. Also, the Interface force field (Heinz *et*  
449 *al.*, 2013) which includes explicit bonding between surface atoms and dissimilar atom types for  
450 basal oxygen atoms, may be more suited to this task.

451

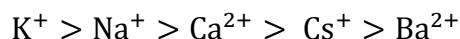
452 ***Equilibrium Constants and Determining a Hofmeister Series for the basal surface of***

453 ***Montmorillonite:***

454 To compare binding energies between divalent and monovalent cations at basal surfaces  
455 it is required to divide the divalent binding affinity by two (or double the monovalent value)  
456 since it takes two monovalent ions to replace a single divalent ion in identical clay systems. This



457 is valid assuming that the chemical environments of the two monovalent ions do not overly  
458 interact with one another. Following this procedure, the results present a Hofmeister-like series  
459 for ion adsorption to smectite mineral surfaces of the form:



460 Furthermore, the binding energy difference between ion A and B ( $\Delta\Delta G_A^B$ ) can be  
461 tabulated by considering the difference in global binding energies between the respective atoms  
462 (Table 4). These values are related to the exchange equilibrium constant ( ${}^{ex}K_A^B$ ) as (Bourg and  
463 Sposito, 2011):

464  $\Delta\Delta G = -RT \ln(K)$  (6) where  ${}^{ex}K_A^B$  relates to the equilibrium reaction  
465 between clay, cation A and cation B:

466  $A - \text{Clay} + B^+ \rightleftharpoons B - \text{Clay} + A^+$  (7) The calculated equilibrium constants  
467 generally agree with the literature values (Table 5). The  $\Delta\Delta G_A^B$  binding energy differences are of  
468 the order of the thermal energy at 300K (2.476kJ) or smaller in all instances. Overall, the values  
469 of  $K_A^B$  and  $\Delta\Delta G_A^B$  show that the basal surface of montmorillonite is weakly selective, in  
470 agreement with literature results (Bourg and Sposito, 2011).

471

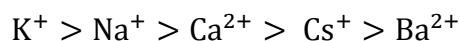
## 472 CONCLUSIONS

473 In this study multiple ensembles of molecular dynamic simulations used in conjunction  
474 with well-tempered metadynamics, have been used to form the basis for deriving the adsorption  
475 energies and mechanisms of simple ions to hydrated mineral surfaces. The methodology is robust  
476 and can be transferred to a wide variety of applications to measure the affinity between mineral  
477 surfaces and a marked assortment of organic material. The results immediately suggest further  
478 ways to improve the accuracy of the calculation of binding energies to clay mineral surfaces.

479 When calculating the binding energy of poorly hydrating molecules to clay surfaces, such as  
480 potassium and cesium, it is critically important to accurately portray the ditrigonal coordination  
481 of basal surface oxygens on the siloxane surface.

482 Detailed analysis of the water structure and planar  $xy$  density of cations in their  
483 energetically favorable states has revealed four separate surface-ion complexations. Both  
484 primary and secondary ISSCs are observed for the weakly and strongly hydrated cations  
485 respectively. A second hydration shell surface complex, whereby the second hydration shell of  
486 the cation overlaps with the first hydration layer of the mineral surface, is observed for sodium.  
487 Outer-shell surface complexes are observed to form for the strongly hydrated ions, sodium,  
488 barium and calcium.

489 Using the metadynamic algorithm, the results have confirmed the idea of a Hofmeister  
490 series for smectite-like minerals. For basal surfaces, the series follows the form:



491 and this insight impacts upon a wide range of industrial applications of clay minerals.  
492 Finally, the preference for monovalent ions to be adsorbed to the surface over the naturally  
493 occurring divalent ions is important for many industrial applications using the cation-exchange  
494 mechanism, whereby an inherently present divalent calcium ion is replaced with monovalent  
495 cation which can improve, for example, water-wettability, and thus increase oil extraction rates  
496 in enhanced oil recovery. Future work entails studying the adsorption of ions as a function of salt  
497 concentration, the energetics of intercalated ions as well as the calculating the energy barriers at  
498 clay edge sites. Furthermore, the role of tetrahedral substitutions may play a large role in the  
499 stability of such ionic systems.  
500

501

**ACKNOWLEDGEMENTS**

502 The authors thank BP for funding Thomas Underwood, the Leverhulme Foundation for funding  
503 Valentina Erastova and the Royal Society for funding H. Chris Greenwell. The work could not  
504 have been completed without the use of Durham University's high-performance computing  
505 services.

506 **BIBLIOGRAPHY**

- 507 Aqvist, J. (1990). Ion-water interaction potentials derived from free energy perturbation  
508 simulations. *The Journal of Physical Chemistry*, **94**, 8021-8024.
- 509 Barducci, A., Bussi, B. and Parrinello M. (2008). Well-Tempered Metadynamics: A Smoothly  
510 Converging and Tunable Free energy Method. *Physical Review Letters*, **100**, 020603.
- 511 Benson, L.V. (1982). A tabulation and evaluation of ion exchange data on smectites.  
512 *Environmental Geology*, **4**, 23-29.
- 513 Berendsen, H.J.C, Grigera, J.R. and Straatsma, T.P. (1987). The missing term in effective pair  
514 potentials. *The Journal of Physical Chemistry*, **91**, 6269–6271.
- 515 Bergaya, F., Theng, B. and Lagaly, G. (2006). *Handbook of Clay Science (Vol. 1)*. Elsevier  
516 Science.
- 517 Boek, E.S., Coveney, P.V. and Skipper, N.T. (1995). Monte Carlo Molecular Modeling Studies of  
518 Hydrated Li-, Na-, and K-Smectites: Understanding the Role of Potassium as a Clay  
519 Swelling Inhibitor. *The Journal of the American Chemical Society*, **117**, 12608–12617.
- 520 Boek, E.S. and Sprik, M. (2003). Ab initio molecular dynamics study of the hydration of a  
521 sodium smectite clay. *The Journal of Physical Chemistry B*, **107**, 3251-3256.
- 522 Bonomi, M., Branduardi, D., Bussi, G., Camilloni, C., Provasi, D., Raiteri, P., Donadio, D.,  
523 Marinelli, F., Pietrucci, F., Broglia, R.A. and Parrinello, M. (2009). PLUMED: A portable  
524 plugin for free energy calculations with molecular dynamics. *Computer Physics*  
525 *Communications*, **180**, 1961-1972.
- 526 Bowers, G.M., Bish, D.L. and Kirkpatrick, R.J. (2008). H<sub>2</sub>O and cation structure and dynamics  
527 in expandable clays: 2H and 39K NMR investigations of hectorite. *The Journal of*  
528 *Physical Chemistry C*, **112**, 6430-6438.

- 529 Bourg I.C. and Sposito G. (2011). *Ion exchange phenomena; Handbook of Soil Science,*  
530 *Properties and Processes (2<sup>nd</sup> Ed.).* CRC Press, Boca Raton.
- 531 Brown, D.R. and Kevan, L. (1988). Aqueous coordination and location of exchangeable copper  
532 (2+) cations in montmorillonite clay studied by electron spin resonance and electron spin  
533 echo modulation. *Journal of the American Chemical Society*, **110**, 2743-2748.
- 534 Chang, F.R.C., Skipper, N.T. and Sposito, G. (1995). Computer simulation of interlayer  
535 molecular structure in sodium montmorillonite hydrates. *Langmuir*, **11**, 2734-2741.
- 536 Chen, C.C. and Hayes, K.F. (1999). X-ray absorption spectroscopy investigation of aqueous Co  
537 (II) and Sr (II) sorption at clay–water interfaces. *Geochimica et Cosmochimica Acta*, **63**,  
538 3205-3215.
- 539 Coveney, P.V. and Wan, S. (2016). On the calculation of equilibrium thermodynamic properties  
540 from molecular dynamics. *Physical Chemistry Chemical Physics*, **DOI:**  
541 10.1039/C6CP02349E.
- 542 Cygan, R.T., Liang, J.J. and Kalinichev, A.G. (2004). Molecular Models of Hydroxide,  
543 Oxyhydroxide, and Clay Phases and the Development of a General Force Field. *The*  
544 *Journal of Physical Chemistry B*, **108**, 1255-1266.
- 545 Downs, R.T. and Hall-Wallace, M. (2003). The American Mineralogist crystal structure database.  
546 *American Mineralogist*, **88**, 247-250.
- 547 Eisenman, G. (1962). Cation selective glass electrodes and their mode of operation. *Biophysical*  
548 *Journal*, **2**, 259-323.
- 549 Gast, R.G. (1972). Alkali metal cation exchange on Chambers montmorillonite. *Soil Science*  
550 *Society of America Journal*, **36**, 14-19.

- 551 Gast, R.G. (1969). Standard free energies of exchange for alkali metal cations on Wyoming  
552 bentonite. *Soil Science Society of America Journal*, **33**, 37-41.
- 553 Greathouse, J.A., Refson, K. and Sposito, G. (2000). Molecular dynamics simulation of water  
554 mobility in magnesium-smectite hydrates. *Journal of the American Chemical Society*,  
555 **122**, 11459-11464.
- 556 Greathouse, J.A., Hart, D.B., Bowers, G.M., Kirkpatrick, R.J. and Cygan, R.T. (2015). Molecular  
557 Simulation of Structure and Diffusion at Smectite–Water Interfaces: Using Expanded  
558 Clay Interlayers as Model Nanopores. *The Journal of Physical Chemistry C*, **119**, 17126–  
559 17136.
- 560 Greenwell, H.C., Jones, W., Coveney, P.V. and Stackhouse, S. (2006). On the application of  
561 computer simulation techniques to anionic and cationic clays: A materials chemistry  
562 perspective. *Journal of Materials Chemistry* , **16**, 708-723.
- 563 Hanshaw, B.B. (1964). Cation-exchange constants for clays from electrochemical measurements.  
564 *12<sup>th</sup> Annual Meeting of the Clay Minerals Society*.
- 565 Heinz, H., Lin, T.-J., Mishra, R.K. and Emami, F.S. (2013). Thermodynamically Consistent  
566 Force Fields for the Assembly of Inorganic, Organic, and Biological Nanostructures: The  
567 INTERFACE Force Field. *Langmuir*, **29**, 1754-1765.
- 568 Hunter, J.D. (2007). Matplotlib: A 2D graphics environment. *Computing in Science and*  
569 *Engineering*, **9**, 90-95.
- 570 Koneshan, S., Lynden-Bell, R.M. and Rasaiah, J.C. (1998). Friction Coefficients of Ions in  
571 Aqueous Solution at 25 °C. *The Journal of the American Chemical Society*, **120**, 12041-  
572 12050.

- 573 Marry, V. and Turq, P. (2003). Microscopic simulations of interlayer structure and dynamics in  
574 bihydrated heteroionic montmorillonites. *The Journal of Physical Chemistry B*, **107**,  
575 1832-1839.
- 576 Marry, V., Dubois, E., Malikova, N., Breu, J. and Haussler, W. (2013). Anisotropy of water  
577 dynamics in clays: insights from molecular simulations for experimental QENS analysis.  
578 *The Journal of Physical Chemistry C*, **117**, 15106-15115
- 579 Michaud-Agrawal, N., Denning, E.J., Woolf, T.B. and Beckstein, O. (2011). MDAnalysis: a  
580 toolkit for the analysis of molecular dynamics simulations. *Journal of Computational*  
581 *Chemistry*, **32**, 2319-2327.
- 582 Nakano, M., Kawamura, K. and Ichikawa, Y. (2003). Local structural information of Cs in  
583 smectite hydrates by means of an EXAFS study and molecular dynamics simulations.  
584 *Applied Clay Science*, **23**, 15-23.
- 585 Ngouana W., B.F. and Kalinichev, A.G. (2014). Structural Arrangements of Isomorphic  
586 Substitutions in Smectites: Molecular Simulation of the Swelling Properties, Interlayer  
587 Structure, and Dynamics of Hydrated Cs–Montmorillonite Revisited with New Clay  
588 Models. *The Journal of Physical Chemistry C*, **118**, 12758-12773.
- 589 Papelis, C. and Hayes, K.F. (1996). Distinguishing between interlayer and external sorption sites  
590 of clay minerals using X-ray absorption spectroscopy. *Colloids and Surfaces A:*  
591 *Physicochemical and Engineering Aspects*, **107**, 89-96.
- 592 Park, S.H. and Sposito, G. (2002). Structure of water adsorbed on a mica surface. *Physical*  
593 *Review Letters*, **89**, 085501.
- 594 Pronk, S., Páll, S., Schulz, R., Larsson, P., Bjelkmar, P., Apostolov, R., Shirts, M.R., Smith, J.C.,  
595 Kasson, P.M., van der Spoel, D. and Hess, B. (2013). GROMACS 4.5: a high-throughput

- 596 and highly parallel open source molecular simulation toolkit. *Bioinformatics*, **29**, 845-  
597 854.
- 598 Rotenberg, B., Marry, V., Malikova, N. and Turq, P. (2010). Molecular simulation of aqueous  
599 solutions at clay surfaces. *Journal of Physics: Condensed Matter*, **22**, 284114.
- 600 Rotenberg, B., Marry, V., Vuilleumier, R., Malikova, N., Simon, C. and Turq, P. (2007). Water  
601 and ions in clays: Unraveling the interlayer/micropore exchange using molecular  
602 dynamics. *Geochimica et Cosmochimica Acta*, **71**, 5089-5101.
- 603 Rotenberg, B., Morel, J.-P., Marry, V., Turq, P. and Morel-Desrosiers, N. (2009). On the driving  
604 force of cation exchange in clays: Insights from combined microcalorimetry experiments  
605 and molecular simulation. *Geochimica et Cosmochimica Acta*, **73**, 4034-4044.
- 606 Strawn, D.G. and Sparks, D.L. (1999). The use of XAFS to distinguish between inner-and outer-  
607 sphere lead adsorption complexes on montmorillonite. *Journal of Colloid and Interface  
608 Science*, **216**, 257-269.
- 609 Shroll, R.M. and Smith, D.E. (1999). Molecular dynamics simulations in the grand canonical  
610 ensemble: Application to clay mineral swelling. *The Journal of Chemical Physics*, **111**,  
611 9025-9033.
- 612 Smith, D.E. and Dang, L.X. (1994). Computer simulations of cesium-water clusters: Do ion-  
613 water clusters form gas-phase clathrates? *The Journal of Chemical Physics*, **101**, 7873.
- 614 Smith, D.E. and Dang, L.X. (1994). Computer simulations of NaCl association in polarizable  
615 water. *The Journal of Chemical Physics*, **100**, 3757.
- 616 Suter, J.L., Anderson, R.L., Greenwell, H.C. and Coveney, P.V. (2009). Recent advances in large-  
617 scale atomistic and coarse-grained molecular dynamics simulation of clay minerals.  
618 *Journal of Materials Chemistry*, **19**, 2482-2493.



- 619 Swenson, J., Bergman, R. and Howells, W.S. (2000). Quasielastic neutron scattering of two-  
620 dimensional water in a vermiculite clay. *The Journal of Chemical Physics*, **113**, 2873-  
621 2879
- 622 Teppen, B.J. and Miller, D.M. (2006). Hydration Energy Determines Isovalent Cation Exchange  
623 Selectivity by Clay Minerals. *Soil Science Society of America Journal*, **70**, 31-40.
- 624 Tesson, S., Salanne, M., Rotenberg, B., Tazi, S. and Marry, V. (2016). Classical Polarizable Force  
625 Field for Clays: Pyrophyllite and Talc. *The Journal of Physical Chemistry C*, **120**, 3749-  
626 3758.
- 627 Tribello, G.A., Bonomi, M., Branduardi, D., Camilloni, C. and Bussi, G. (2014). PLUMED 2:  
628 New feathers for an old bird. *Computer Physics Communications*, **185**, 604-613.
- 629 Underwood, T., Erastova, V., Cubillas, P. and Greenwell, H.C. (2015). Molecular Dynamic  
630 Simulations of Montmorillonite–Organic Interactions under Varying Salinity: An Insight  
631 into Enhanced Oil Recovery. *The Journal of Physical Chemistry C*, **119**, 7282–7294.
- 632 Viani, A., Gualtieri, A.F. and Artioli, G. (2002). The nature of disorder in montmorillonite by  
633 simulation of X-ray powder patterns. *American Mineralogist* , **87**, 966-975.
- 634 William Humphrey, A.D. (1996). VMD: visual molecular dynamics. *Journal of Molecular  
635 Graphics*, **14**, 33-38.
- 636 Zhang, P.C., Brady, P.V., Arthur, S.E., Zhou, W.Q., Sawyer, D. and Hesterberg, D.A. (2001).  
637 Adsorption of barium (II) on montmorillonite: an EXAFS study. *Colloids and Surfaces A:  
638 Physicochemical and Engineering Aspects*, **190**, 239-249.
- 639 Zhang, Y. and Cremer, P.S. (2006). Interactions between macromolecules and ions: the  
640 Hofmeister series. *Current Opinion in Chemical Biology*, **10**, 658-663.
- 641

642 Table 1

643 *Binding energies and stable clay-ion separations of cations to montmorillonite basal surfaces. The global energy minimum for each*  
 644 *ion is bolded. Clay-ion separation values are given in Angstrom and Binding Energies are in kJ/mol. The Primary ISSC is defined as*  
 645 *the inner-sphere complex located above the hexagonal siloxane cavity of the clay, whilst the secondary ISSC is the complex above a*  
 646 *basal surface oxygen.*

647

Ion	VdW Radii	Primary ISSC		Secondary ISSC		OSSC		SHSSC	
		Separation	Energy	Separation	Energy	Separation	Energy	Separation	Energy
Na <sup>+</sup>	2.35	-		2.3	-2.76 (0.43)	<b>3.8</b>	<b>-9.00 (0.35)</b>	6.0	-3.68 (0.37)
K <sup>+</sup>	3.33	<b>1.3</b>	<b>-10.56 (1.29)</b>	2.6	-2.46 (0.70)	4.7	-3.83 (0.37)	-	
Cs <sup>+</sup>	3.83	<b>2.0</b>	<b>-8.34 (0.40)</b>	2.7	-7.51 (0.38)	4.6	-4.64 (0.26)	-	
Ca <sup>2+</sup>	2.87	-		-		<b>3.8</b>	<b>-16.76 (0.41)</b>	-	
Ba <sup>2+</sup>	3.81	1.9	+18.26 (3.55)	2.6	-0.54 (1.82)	<b>4.2</b>	<b>-16.66 (1.46)</b>	5.8	-8.38 (1.25)

648

649

650 Table 2

651 *The atomic radii and therefore charge to size ratio for each ion. The hydrated radii are calculated as the first minima in the RDF of*  
 652 *each respective ion. The stable surface complex of each ion is linked to the size of the ion's hydration radii and thus charge to size*  
 653 *ratio.*

654

Ion	Atomic Radii	Charge/Size ratio	Hydrated Radii	Stable Complex
Na <sup>+</sup>	1.90	0.53	3.23	OSSC
K <sup>+</sup>	2.43	0.41	3.83	ISSC
Cs <sup>+</sup>	2.98	0.34	3.87	ISSC
Ca <sup>2+</sup>	1.94	1.03	3.13	OSSC
Ba <sup>2+</sup>	2.53	0.79	3.49	OSSC

Table 3

The coordination number of each ion in each surface complexation state. Expected coordination numbers are taken from (Varma, 2006).

Species	Expected CN	Observed CN	Clay CN	Water CN	Percentage Clay	Percentage Water
<b>Primary ISSC</b>						
Na <sup>+</sup>	5	-	-	-	-	-
K <sup>+</sup>	6	9.3	5.9	3.4	64%	36%
Cs <sup>+</sup>	7	11.8	5.9	5.9	50%	50%
Ca <sup>2+</sup>	5-7	-	-	-	-	-
Ba <sup>2+</sup>	5-7	8.5	1.1	7.4	13%	87%
<b>Secondary ISSC</b>						
Na <sup>+</sup>	5	5.9	1.1	4.8	19%	81%
K <sup>+</sup>	6	7.6	1.9	5.7	25%	75%
Cs <sup>+</sup>	7	9.4	2.7	6.7	29%	71%
Ca <sup>2+</sup>	5-7	-	-	-	-	-
Ba <sup>2+</sup>	5-7	8.5	1.1	7.4	13%	87%
<b>OSSC</b>						
Na <sup>+</sup>	5	5.9	0	5.9	0%	100%
K <sup>+</sup>	6	7.6	0	7.6	0%	100%
Cs <sup>+</sup>	7	9.3	0	9.3	0%	100%
Ca <sup>2+</sup>	5-7	8	0	8	0%	100%
Ba <sup>2+</sup>	5-7	9	0	9	0%	100%
<b>SHSSC</b>						
Na <sup>+</sup>	5	5.8	0	5.8	0%	100%
K <sup>+</sup>	6	-	-	-	-	-
Cs <sup>+</sup>	7	-	-	-	-	-
Ca <sup>2+</sup>	5-7	8	0	8	0%	100%
Ba <sup>2+</sup>	5-7	9	0	9	0%	100%
<b>Bulk</b>						
Na <sup>+</sup>	5	5.9	0	5.9	0%	100%
K <sup>+</sup>	6	7.8	0	7.8	0%	100%
Cs <sup>+</sup>	7	8.2	0	8.2	0%	100%
Ca <sup>2+</sup>	5-7	8	0	8	0%	100%
Ba <sup>2+</sup>	5-7	9	0	9	0%	100%

**Table 4**

The binding energy difference ( $\Delta\Delta G_A^B$ ) between ion species.

$\Delta\Delta G_A^B$	Na <sup>+</sup>	K <sup>+</sup>	Cs <sup>+</sup>	Ca <sup>2+</sup>	Ba <sup>2+</sup>
Na <sup>+</sup>	<b>0.00</b>	-1.56	0.66	0.62	0.67
K <sup>+</sup>	1.56	<b>0.00</b>	2.22	2.18	2.23
Cs <sup>+</sup>	-0.66	-2.22	<b>0.00</b>	-0.04	0.01
Ca <sup>2+</sup>	-0.62	-2.18	0.04	<b>0.00</b>	0.05
Ba <sup>2+</sup>	-0.67	-2.23	-0.01	-0.05	<b>0.00</b>

**Table 5**

The exchange equilibrium constants ( ${}^{\text{ex}}K_A^B$ ) for each ion exchange reaction. Literature values are presented in bold italics (Bourg and Sposito, 2011) (Benson, 1982).

${}^{\text{ex}}K_A^B$	Na <sup>+</sup>	K <sup>+</sup>	Cs <sup>+</sup>	Ca <sup>2+</sup>	Ba <sup>2+</sup>
Na <sup>+</sup>	-	1.87	0.77	0.78	0.76
K <sup>+</sup>	0.54 <b>0.58</b>	-	0.41	0.42	0.41
Cs <sup>+</sup>	1.30 <b>1.23</b>	2.44	-	1.02	1.00
Ca <sup>2+</sup>	1.28 <b>1.21</b>	2.40 <b>1.04</b>	0.98 <b>0.26</b>	-	0.98
Ba <sup>2+</sup>	1.31 <b>1.44</b>	2.45	1.00	1.02	-

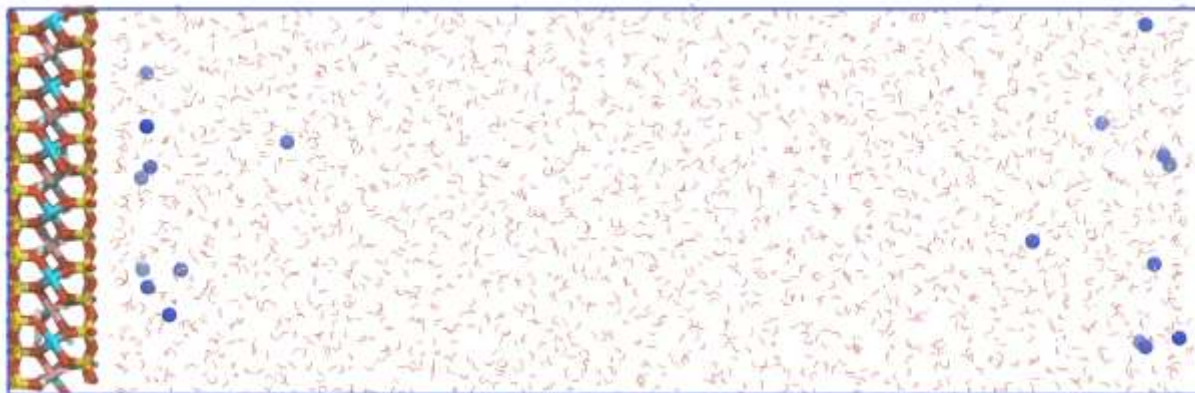


*Figure 1: An example supercell used in the simulations. This example is of sodium cations (dark blue) interacting with montmorillonite. The color scheme of the clay is as follows: Silicons are yellow; oxygens are red; aluminums are blue; magnesiums are pink and hydrogens are white. Also presented in stick form are the water molecules within the nano-pore spacing. Periodic boundaries are used in all directions, and the simulation supercell has dimensions approximately  $4 \times 4 \times 10$  nm (note that the figure is flipped here, such that the z-direction is across the page, from left to right).*

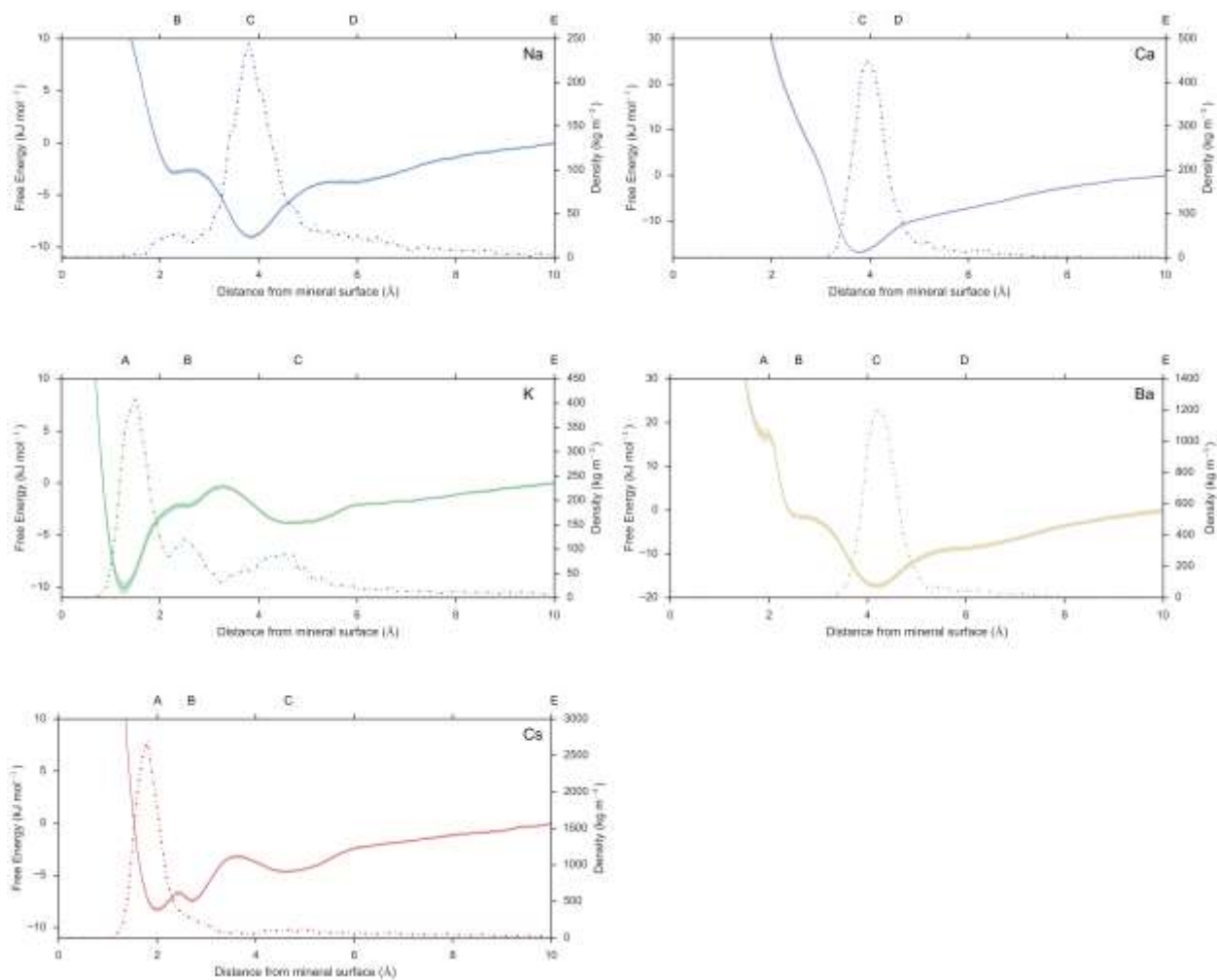


Figure 2: The free energy profile of all cations as a function of clay-ion separation. Note that the shaded region indicates the standard error in the metadynamic calculation at each point along the free-energy diagram. Also presented is the ion density as a function of distance from clay basal surface (dotted line). The points (A), (B), (C) and (D) are noted as interesting features within the free-energy diagram and are shown at the top of the figure.

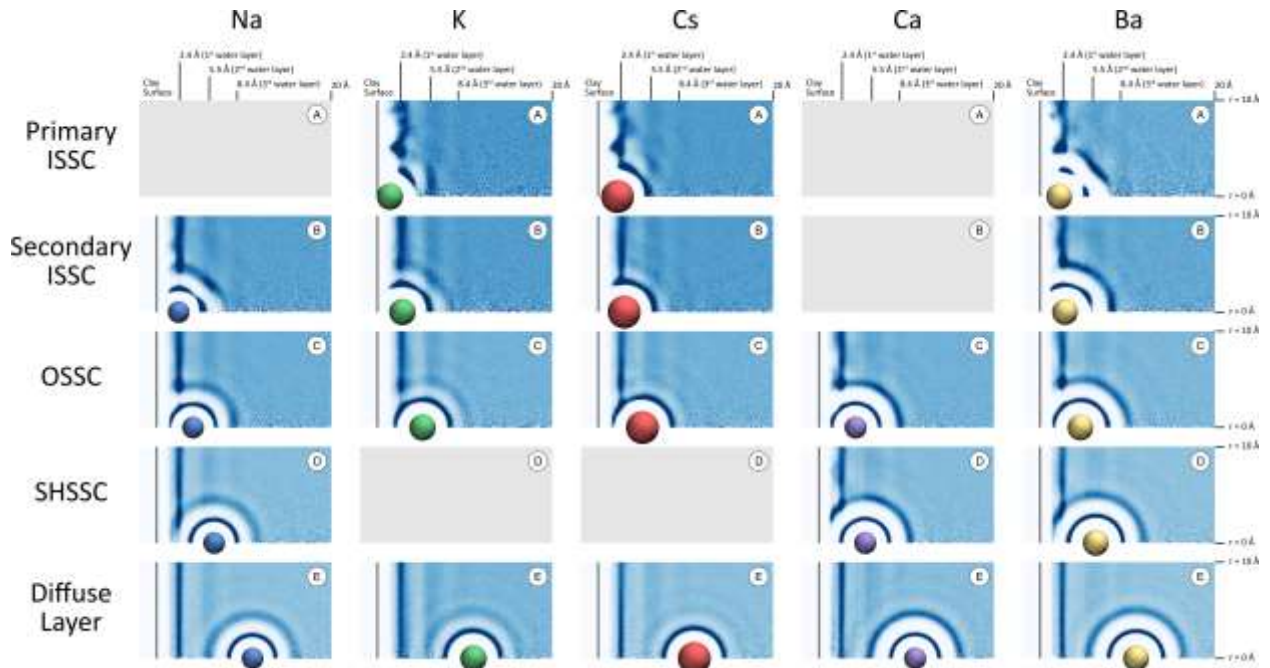


Figure 3: The water oxygen density surrounding the clay and ion at point of interest along the free-energy curve.

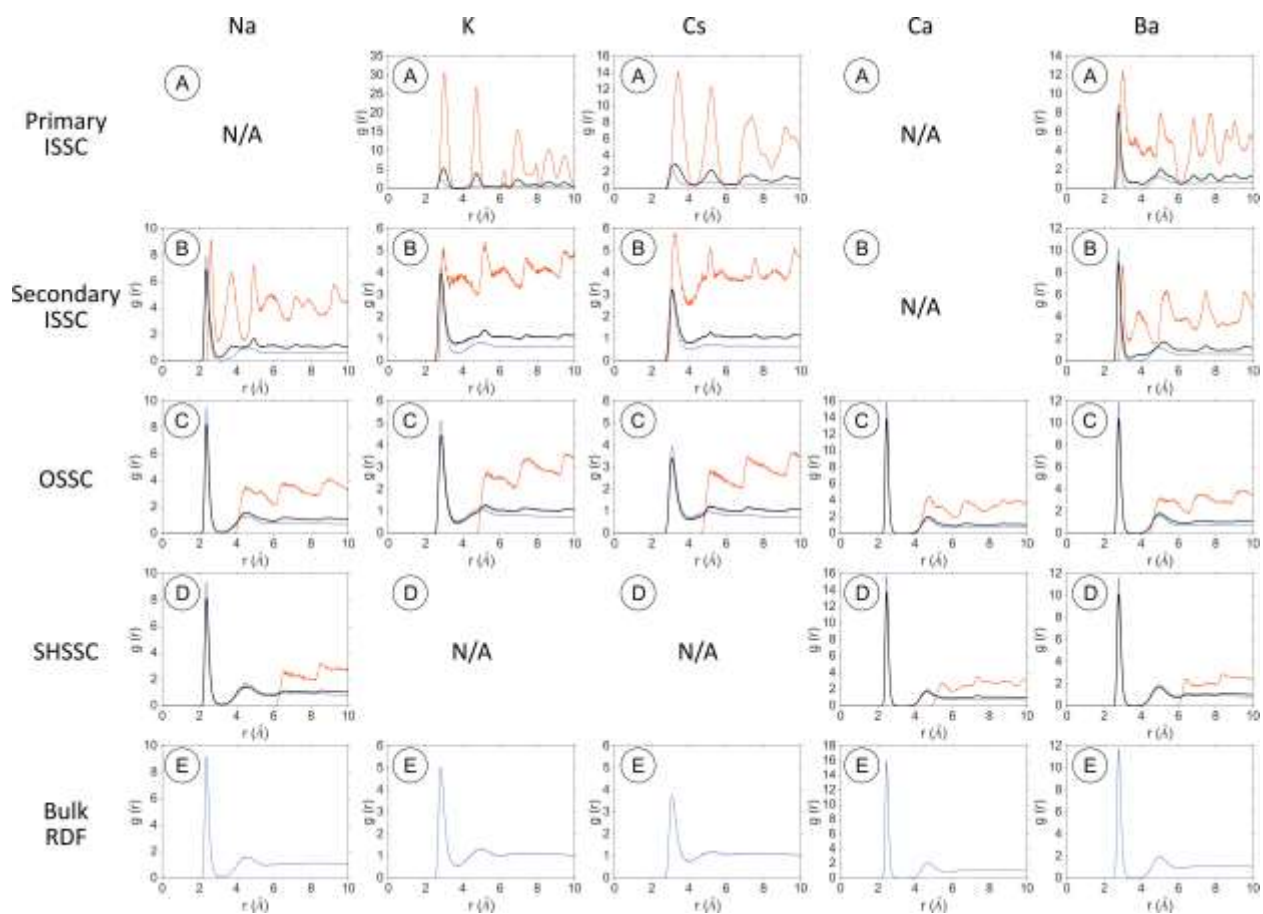


Figure 4: The RDF's between each cation and oxygen atoms at each point of interest along the free-energy diagram. Blue is the RDF between cation and water oxygen, orange is between cation and clay oxygen, and black is the RDF between cation and all oxygen atoms.



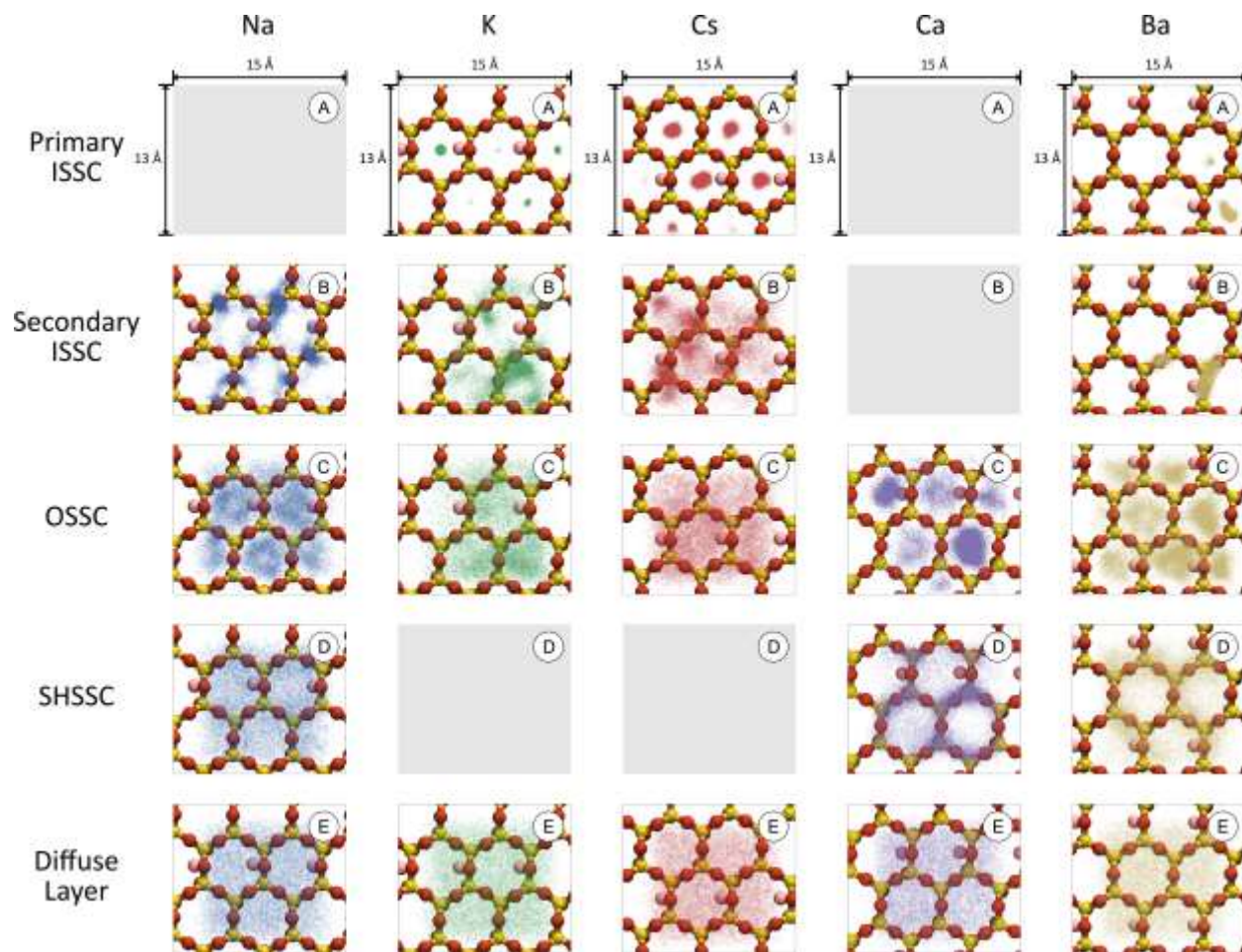


Figure 5: The xy-planar density of the examined cations at each point of interest along the free energy curve.

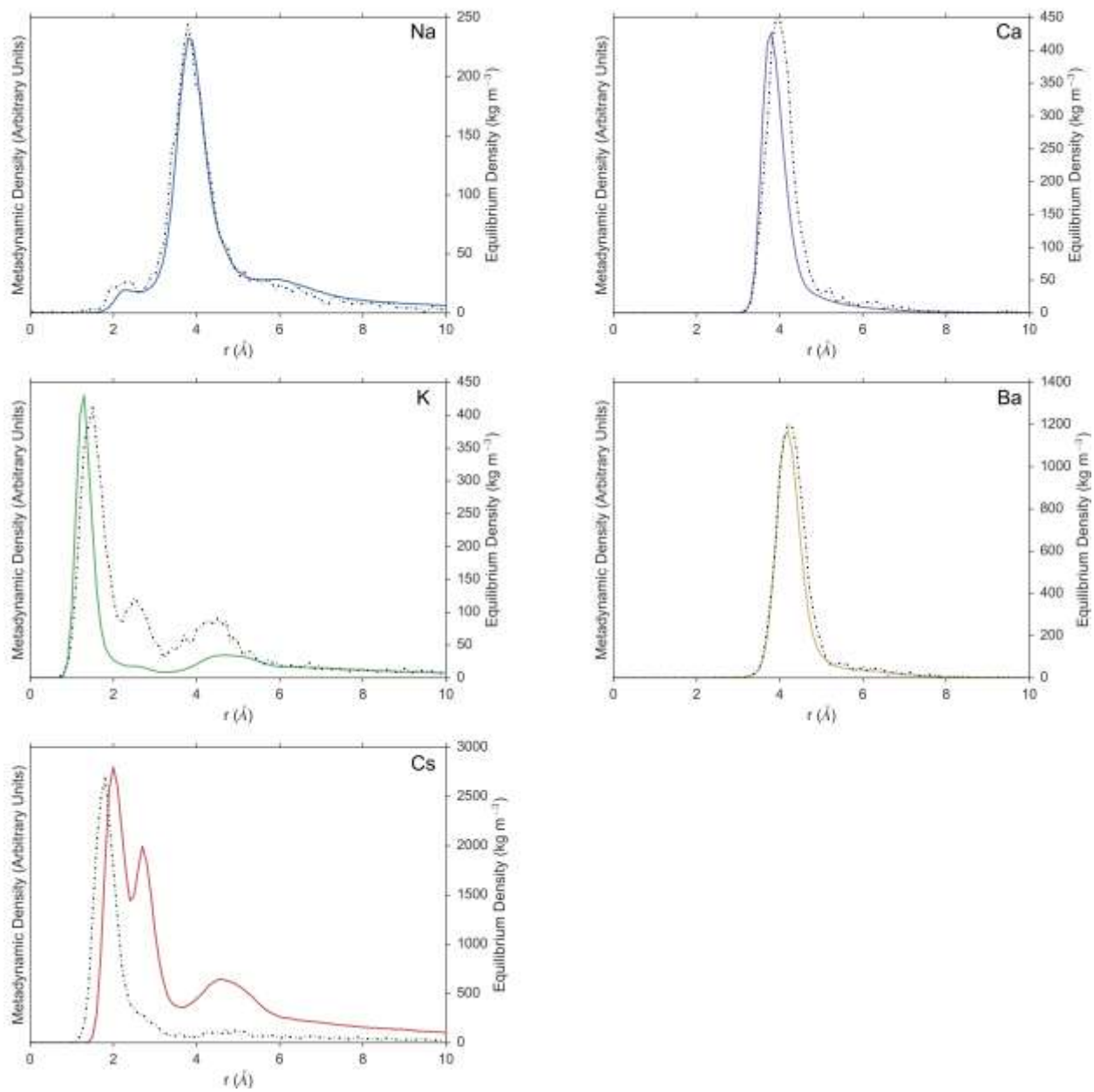


Figure 6: A comparison of ionic densities surrounding the clay surface. Bold colored line is the density calculated from the free energy profile, and the dotted line is the density calculated from an unbiased simulation.